10-2019

Self-Assembling of Graphene Oxide on Carbon Quantum Dot Loaded Liposomes

Mohadeseh Hashemi
University of Tehran, Tehran, Iran

Javad Mohammadi
University of Tehran, Tehran, Iran

Meisam Omidi
Shahid Beheshti University

Hugh D.C. Smyth
University of Texas at Austin

Bharadwaj Muralidharan
University of Texas at Austin

See next page for additional authors

Materials Science and Engineering : C, Vol. 103 (October 2019): 109860. DOI.

Self-Assembling of Graphene Oxide on Carbon Quantum Dot Loaded Liposomes

Mohadeseh Hashemi
Department of Biomedical Engineering, The University of Texas at Austin, Austin
Division of Pharmaceutics, College of Pharmacy, The University of Texas at Austin
Department of Biomedical Engineering, Faculty of New Science and Technology, The University of Tehran, Iran
Javad Mohammadi
Department of Biomedical Engineering, Faculty of New Science and Technology, The University of Tehran, Iran
Meisam Omidi
Protein Research Center, Shahid Beheshti University, GC, Tehran, Iran
Department of Developmental Sciences, Marquette University School of Dentistry, Milwaukee
Hugh D.C. Smyth
Division of Pharmaceutics, College of Pharmacy, The University of Texas at Austin
Bharadwaj Muralidharan
Department of Biomedical Engineering, The University of Texas at Austin, Austin
Thomas E. Milner

Department of Biomedical Engineering, The University of Texas at Austin, Austin
Amir Yadegari
Department of Developmental Sciences, Marquette University School of Dentistry, Milwaukee
Davoud Ahmadvand
School of Allied Medical Sciences, Iran University of Medical Sciences, Tehran, Iran
Mohammad Shalbaf
South Tehran Branch, Islamic Azad University, Tehran, Iran
Lobat Tayebi
Department of Developmental Sciences, Marquette University School of Dentistry, Milwaukee

Abstract

This paper describes the design of stimuli-sensitive theranostic nanoparticles, composed of reduced graphene oxide (rGO) self-assembled on thermosensitive liposomes encapsulated doxorubicin (DOX) and carbon quantum dot (CQD) (CQD-DOX-rGO-Tlip). The rGO-Tlip particles have been observed to be flower-shaped objects. The thermoresponsive and theranostic potential of CQD-DOX-rGO-Tlips have been studied using differential scanning calorimetry (DSC), ultraviolet visible spectroscopy (UV–Vis), Raman spectroscopy and photoluminescent assays. The chemo-photothermal potential of rGO–Tlip on MD-MB-231 cells during NIR laser irradiation has been examined using MTT assay. Also, the ability of rGO–Tlip to be taken up by MD-MB-231 cells has been studied using confocal microscopy and flowcytometry. The results indicate that CQD-DOX-rGO-Tlips achieve a synergistic effect between photothermal therapy and chemotherapy for cancer treatment. Furthermore, online monitoring drug release is accomplished by studying the emission intensity of CQD while DOX released.

Keywords

Reduced graphene oxide, Liposomes, Carbon quantum dot, Chemotherapy, Photothermal therapy

1. Introduction

Theranostic, integration of both diagnostic and therapy approach into a single platform, are of significant interest in clinically relevant cancer models [1]. As a long standing problem of conventional chemotherapy is the lack of tumor specificity [2], theranostic systems have drawn a particular interest by integrating imaging probes and chemotherapeutic drugs into a single system [3,4]. The emergence of stimuli-sensitive nanoparticles brings a new perspective for theranostic system. Stimuli-sensitive systems release the load at desired sites, activated by either external stimuli including light, ultrasound, magnetic fields, and electric fields [[5], [6], [7]] or internal stimuli such as redox potential, pH levels, and different enzymatic conditions [[8], [9], [10]].

Among these stimuli, triggering drug release using near infrared (NIR) light has demonstrated some advantages. This is because light in NIR region penetrates deeper into the tissue, and the main NIR light-tissue interaction include absorption and scattering [11,12]. Thus, over the last decade or so, several types of photo-absorbers with optical absorption in the NIR range have been investigated, such as gold nanoshells [13], gold nanorods [[14], [15], [16], [17]], carbon nanotubes [[18], [19], [20], [21]], and graphene oxide [22,23]. As a hyperthermia agent, graphene oxide (GO) has received significant interest in the nanocarbon research area [[24], [25], [26], [27]].

GO, a two-dimensional sp^2 and sp^3-bonded carbon atoms that are organized in a hexagonal lattice structure, can absorb NIR due to the delocalization of its electron arrangement. This absorbed NIR can then be transformed into thermal energy [22,24,28]. GO is considered a versatile triggering agent in chemo-photothermal therapy application because it has a high aspect ratio, a large number of functional groups on its surface, low production cost, and acceptable thermal conductivity [24,29,30].

Although studies demonstrate that rGO has better photothermal performance than GO, the use of rGO has been limited by its poor water solubility due to the lack of hydrophilic groups on its surface [31]. Furthermore, reducing surface functional groups results in decreasing available drug binding sites. To overcome these obstacles, Zhang et al. showed that modification of rGO with polyethylene glycol (PEG) can deliver ribonucleic acid (RNA) to cancer cells [32]. Imani et al. utilized a noncovalent method to modify the surface of rGO with phospholipid-polyethylene glycol, polystyrene-*co*-polyacrylic acid, and polystyrene-*co*-poly 4-vinylpyridine [33]. Hashmi et al. conjugated R9 and Arginine peptide to the surface of reduced GO to improve dispensability and cellular uptake by the cancer cell line [34,35]. Encapsulating hydrophobic rGO in a nanoparticle increased solubility of poorly soluble rGO sheets in an aqueous solution. For example, Yang et al. prepared a chitosan-based nanocomposite encapsulation of rGO and nickel as a biosensor for screening glucose [36]. Due to the established role of liposomes to deliver chemotherapeutic drug and rGO in photothermal therapy, we propose that a composite of both will have excellent chemo-photothermal properties.

Drug nanocarriers systems with the capability of controlled drug release [37], dual therapy [6] and cancer diagnosis [37] which meet the criteria of modern therapy has revived interest in recent years. Furthermore, effective technique for online monitoring of drug release, for optimizing drug dosage to achieve effective treatment, has gained great attention. Necessitated by monitored drug release, carbon quantum dots (CQDs) have drawn considerable attention due to their high biocompatibility, good solubility, broad optical absorption and intense photoluminescence (PL) [38].

CQDs have absorbed great deals of attention in the biomedical applications due to their unique photoluminescence properties, high photostability, exceptional biocompatibility, and excellent physiochemical properties [39]. CQDs being used in wide verity of applications including bioimaging, biosensing, drug/gene delivery, and anticancer agents [39]. For the first time, Sun et al. applied PEG $_{1500N}$ passivated CQDs for cellular imaging [40]. Then, the application of CQDs was further developed for real-time molecular tracking and in vivo imaging. The application of CQDs for in vivo imaging was first reported by Yang et al. [41]. They injected PEG-passivated C-dots intravenously, intradermally, and subcutaneously into mice for fluorescence imaging. In another study, Tao et al. injected CQD into nude mice resulting good contrast [42]. More recently, Liu et al. synthesized dimethyl amine functionalized CQDs with high absorption cross section and low photobleaching effect for deep-tissue imaging [43].

In this study, we describe a novel theranostic stimuli-sensitive system, which is composed of rGO self-assembled into thermosensitive liposome (rGO-Tlip) encapsulating DOX (DOX-rGO-Tlip), as a chemotropic agent, and CQD (CQD-DOX-rGO-Tlip), monitoring drug accumulation and release in tumorigenic region.

First, we prepared thermosensitive liposomes comprised of DPPC/Brij78/Chol. These formulations were optimized using a central composite design (CCD) and a response surface method (RSM) to find an optimized formulation with a minimum drug leakage at physiological temperature and a maximum drug release rate under mild hyperthermia. We characterized rGO using Fourier transform infrared (FTIR) and ultraviolet visible (UV–Vis) spectroscopy. Also, the intensity of NIR light absorption by rGO sheets was evaluated by calculating absorption cross-section of rGO. Then, we investigated the interaction between rGO and liposomes using scanning electron microscope (SEM), Raman, differential scanning calorimeter (DSC), UV–Vis spectra and infrared (IR) camera. Interaction of CQD and DOX inside the nanoparticles and after DOX release was further studied using

photoluminescence (PL) spectrophotometer. Then, in vitro and in vivo evaluation of CQD-DOX-rGO-Tlip on cell and tumor toxicity of breast cancer was studied. In addition, we investigated the cellular uptake of CQD-DOX-rGO-Tlip using confocal microscopy and flow cytometry. For further study, in vivo assay was adopted.

2. Materials and methods

2.1. Materials

1,2-dipalmitoyl-sn-glycerol-3-phosphatidylcholine (DPPC) and cholesterol (Chol) were purchased from Avanti Polar Lipids Inc. (Alabaster, AL). Graphene oxide (GO) was purchased from Graphene Supermarket (Reading, MA, USA). Polyoxyethylene (20) stearyl ether (Brij 78), doxorubicin hydrochloride (DOX), potassium hydroxide (KOH), sodium borohydride ($NaBH_4$), phosphate buffer saline (PBS), fetal bovine serum (FBS) and Dulbecco's Modified Eagle Medium (DMEM) and Cell Proliferation Reagent Kit I (MTT) were supplied by Sigma Aldrich (USA). Live/dead cell viability assay kits were purchased from Thermo-Fisher. PE (Lissamine Rhodamine B) was obtained from Avanti Polar Lipids Inc. Cell tracker green was purchased from molecular probe Inc. Mounted media were ordered from Vector Laboratories, CA.

All other chemicals were of analytical grade.

2.2. Methods

2.2.1. Liposome preparation and characterization

Temperature-sensitive liposomes (Tlip) were prepared using the thin film hydration and pH gradient loading methods [44,45]. Preparation and characterization methods are described in detail in Supplementary 1.

2.2.2. Mathematical optimization of drug release rate at 37 °C and 42 °C

To provide maximum drug release during mild hyperthermia (42 °C) and to ensure minimum drug leakage at 37 °C, the Brij 78 and Chol molar ratios in the thermosensitive formation have been optimized using the central composite design (CCD) and response surface (RSM) method which are described in Supplementary 1.

2.2.3. Preparation and characterization of rGO

The aqueous 2 $mg{\cdot}ml^{-1}$ of GO solution was probe sonicated for 3 h (100 W, 5 s on and 2 s off (Misonix, USA)) to decrease the lateral size. Then, reduced graphene oxide (rGO) was obtained by dissolving GO in $NaBH_4$ to obtain a concentration of 1 M in water and was kept overnight at 70 °C. Then, the suspension was washed 5 times with methanol using centrifugation (5000 rpm for 5 min). We conducted UV–Vis-NIR spectroscopy and FTIR analysis to prove rGO formation.

2.2.4. Calculation of absorption cross-section of rGO

The setup comprised of a low power pulsed laser diode as a light source, coupled to an optical fiber (Thorlabs BFL48-1000, USA), emitting at 808 nm. The light was focused by an aspherical condenser lens (with a 20-mm focal length) to a 6 mm diameter spot size on the surface of the sample. The temperature was monitored using Indium antimonide (InSb) IR camera (FLIR ThermaCAM SC3000, USA).

The protocol for the calculation of absorption cross-section, as described by Hashemi et al. [35,45], is provided in Supplementary 3.

2.2.5. Preparation and characterization of CQD

Carbon dots were synthesized through one pot hydrothermal reaction [[46], [47], [48]]. The method is discussed in detail in Supplementary 1.

2.2.6. Preparation of the liposome-reduced GO Nano-assembly (rGO-Tlip)

Thermosensitive liposomal nano-assembled rGO (rGO-Tlip) was synthesized as described in Supplementary 1. Briefly, the optimized formulation, which was composed of DPPC:Chol:Brij 78 (at a molar ratio of 84.82:10.35:4.83) was dissolved in chloroform in a round-bottom flask. Then, various concentrations of an rGO–methanol suspension (0.25, 0.5, 1, and 1.5 $mg{\cdot}ml^{-1}$) were added to the flask and dried under reduced pressure in a rotary evaporator at 37 °C to form a dried lipid film. This lipid film was hydrated with 200 mM of a $(NH_4)_2SO_4$ solution containing CQD at a concentration of 10 µg/ml at 45 °C and pH of 4 (CQD-rGO-Tlip). These multilamellar liposomes were reduced in size using a probe sonicator (under a power of 40 W for 4 min 2 s on and 2 s off (Hitachi Ltd., Tokyo, Japan)). Free CQD were separated using dialysis bag. Then, to separate free rGO from the nanohybrid, the rGO-Tlip was centrifuged at 7500 rpm for 5 min, then washed with PBS five times. The collected platelet was analyzed using UV–Vis spectroscopy (Infinite M200, CA, USA) at a wavelength of 808 nm to calculate the amount of rGO incorporated into the rGO-Tlip. Then, a pH gradient was induced and DOX loading (CQD-DOX-rGO-Tlip) was conducted using the method described in the previous subsection. Dialysis method was used to separate free DOX from the CQD-DOX-rGO-Tlip.

2.2.7. Characterization of rGO-Tlip

As mentioned in Section 2.2.6, the encapsulation efficiency of DOX-rGO-Tlip was calculated at a wavelength of 478 nm using UV–Vis spectroscopy after complete solubilization of the liposome with Triton X-100 (Sigma-Aldrich) using the appropriate concentration of rGO as a blank solution. The Tlip, DOX-Tlip, rGO-Tlip, and DOX-rGO-Tlip were analyzed at various rGO concentrations using an UV–Vis-NIR spectrophotometer. The Raman spectra of the samples were recorded at room temperature at 514 nm excitation using an Alpha 300 spectrometer (WITec, Germany).

Also, the size of the nanoparticles was analyzed using light scattering (Zetasizer Nano ZS, Malvern Instruments, Malvern, UK). The morphology of the hybrid nanoparticles was characterized using a scanning electron microscope (SEM/STEM, Hitachi S-5500, Hitachi Ltd., Japan).

2.2.8. Photoluminescence study of CQD-DOX-rGO-Tlip

The photoluminescence spectroscopy (PL, Infinite M200, Tecan Systems Inc., USA) of DOX, CQD and DOX-rGO-Tlip was carried out with a 280 nm laser excitation. Different mass ratio of CQD/DOX (0.01, 0.05, 0.1, 0.25, 0.5, 1) were prepared by adding appropriate amount of CQD suspension to DOX solution at 25 °C for 12 h in the dark to promote DOX to CQDs binding. Emission intensity at 426 and 600 nm (characteristic emission spectra of CQD and DOX respectively for a 280 nm excitation) of different mass ratio solutions was measured with the PL spectroscopy.

To predict the amount of drug release using CQD, the amount of DOX release at different time intervals were measured as previously explained in Supplementary 1.the emission intensity at 426 and 600 nm, excited at a wavelength of 280 nm, inside the dialysis bag were analyzed using photoluminescent (PL, Infinite M200, Tecan Systems Inc., USA).

2.2.9. In vitro photothermal study of DOX-rGO-Tlip

DOX-rGO-Tlip, with different initial concentrations of rGO (0.25, 0.5, 1, and 1.5 $mg{\cdot}ml^{-1}$), were transferred into the standard 96-well plate. These suspensions, individually, were irradiated by 808 nm pulsed laser, with a repetition rate of 2 Hz and a pulse duration of 250 ms, at different power densities (0.5, 1, 1.5, 3, and 4.2 $W{\cdot}cm^{-2}$) distributed over a spot size of 6 mm on the suspension. The increase in temperature was monitored using an IR camera.

The amount of DOX release in 96-well plate were studied by incubating two groups (a control and a laser group) of DOX-rGO (1)-Tlip (contains 1 $mg{\cdot}ml^{-1}$ of rGO in the initial liposomal formulation) and DOX-Tlip overnight, for

different concentration of DOX (1.25, 2.5, 5, 10, 20 μg. ml^{-1}) in the formulation. The laser group were irradiated by NIR pulsed laser (1 W·cm^{-2}) for 5 min. The intensity of emission at 600 nm was measured using PL spectrometer excited by 280 nm light, for all samples.

The potential chemo-photothermal therapy properties of DOX-rGO-Tlip on MD-MB-231 were evaluated using MTT and live/dead assays. MD-MB-231 cells were seeded at a density of 50,000 cells/well in a 96-well plate and left overnight. Then, the medium in the well was replaced with a fresh medium (complete DMEM) containing one of the three formulations – free DOX, DOX-Tlip and DOX-rGO(1)-Tlip; into two groups (a control and a laser group) for all combinations of different DOX concentrations (0, 1.25, 2.5, 5, 10, and 20 μg·ml^{-1}) in the formulation. The plates were then incubated for 24 h.

After incubation, the cell line in the laser group was exposed to pulsed NIR for 5 min at 1 W·cm^{-2}. To evaluate the cell viability, 10 μl of the MTT assay (5 mg·ml^{-1}) was added to each well and the plate was incubated for additional 4 h. Further, to dissolve formazan crystals, 200 μl of dimethyl sulfoxide was added to each well and was allowed to shake for 20 min [49]. The optical density of each well at 690 nm was 570 (background subtracted), as measured by a microplate reader (Infinite M200, Tecan Systems Inc., USA). The viability of each cell line was calculated using the Eq. (1):

$$(1)\ \text{mean viability} = \frac{\text{mean absorbance value of treatment group} - \text{blank}}{\text{mean absorbance value of control} - \text{blank}} \times 100$$

To visualize the chemo-photothermal potential of DOX-rGO-Tlip, MD-MB-231 cells were stained using live/dead assay. The MD-MB-231 cell line was seeded at a cell density of 50,000 cells/well in 96-well plates and incubated for 24 h before use. The cells were then treated with 100 μl of DOX-rGO(1)-Tlip (100 μg·ml^{-1} of DOX) for 24 h, washed with PBS three times, then exposed to NIR pulse laser irradiation (5 min, 1 W·cm^{-2}). Then, after 1 h, the cells were stained using 2 M of calcein AM and 4 M of ethidium homodimer-1 (EthD–1) for 15 min. Calcein AM converts to fluorescent calcein in living cells (excitation ~495 nm, emission ~515 nm) while EthD–1 (excitation ~495 nm, emission ~635 nm) penetrates in to the damaged cell membrane and attaches to the nucleic acids. Fluorescent images were captured under an inverted fluorescent microscope (Evos, Life Technologies).

2.2.10. Confocal and flow cytometry analysis

The intracellular uptake of CQD-rGO-Tlip into the MD-MB-231 cell line was studied using confocal microscopy (Prairie Technologies, Inc) and flow cytometry (BD LASER Fortessa flow cytometer, Singapore). The MD-MB-231 was cultured in a 6-well plate at a density of 2×10^5 cell/well. After 24 h, cells, with CQD-rGO-Tlip added, were incubated for 0, 4, and 24 h. After incubation, the cells were washed four times with PBS. Intracellular uptake and intracellular binding were monitored using a flow cytometer.

To visualize DOX-rGO-Tlip cellular uptake, cells were stained with a green fluorescent cell tracker probe, at a concentration of 4 μM in DMSO, for 15 min and then washed three times with PBS. Cells were then fixed with 4% paraformaldehyde for 1 h at room temperature. The fixed cells were washed three times with PBS. Cells were mounted using a mounting medium and left at room temperature overnight. The morphology of the cell lines was observed using confocal microscopy.

2.2.11. In vivo assay

In vivo assay were carried out using a protocol provided by Yang et al. [50]. Balb/c mice bearing 4T1 tumors were intratumorally injected with 100 μl of 2 mg/ml of DOX, rGO-Tlip or DOX-rGO-Tlip (n = 7 for each group). For the laser treatment groups (rGO-Tlip, DOX-rGO-Tlip), the tumors of mice were irradiated by a multimodal optical fiber (Thorlabs BFL48-1000, USA) emitting NIR pulsed laser at a power density of 1 W/cm^2 for 5 min. The exact power density was measured using an LPE-1B laser power meter (Physcience OptoElectronics, Beijing). The tumor size was continuously measured by a caliper and calculated.

(2) $V = \frac{(tumor\ length) \times (tumor\ width)^2}{2}$

In Eq. (2), V is a tumor valuate. Elative tumor volume was measured as V/V_0 (V_0 is the initial volume of the tumor before treatment). All the animal experiments were approved by the Animal Ethics Committee, Shahid Beheshti University of Medical Sciences (IR, SBMU.RETECH.REC.1395.291).

2.2.12. Statistical analysis

The results were analyzed using one-way analysis of variance (ANOVA) followed by Tukey's pairwise test at the 5% significance level.

3. Results and discussion

3.1. Evaluation of Tlip formulation

Lysolipid (MSPC) which typically is a crucial component in thermosensitive liposomal formulation in most cases, can affect both the rate and extend of drug release [51]. Thus, a lysolipid-containing thermosensitive liposome (LTSL) is one of the gold standard formulations in this area of research [52,53]. However, concerns have been raised regarding the desorption of lysolipids from LTSL in biological media and the defect formation in the membrane that caused undesirable in vivo drug leakage at physiological temperatures during LTSL blood circulation [54]. As a solution, Tagami et al. developed a new thermoresponsive liposome using a Brij 78 surfactant and substituting MSPC and DSPE-PEG2000 functionality [52]. This simplified formulation, composed of DPPC/Brij 78 (96/4), has enhanced drug release beyond that of LTSL and had led to a 40% increase in drug uptake in equivalent blood pharmacokinetics [52,55]. Although this formulation exhibited better thermal-induced burst release than LTSL, the lack of cholesterol decreases bilayer stability during shelf life and circulation in blood [56,57].

A design of experiments technique was used to optimize liposomal composition. Initial formulations were based on studies by Tagami et al. [55]. In our studies, we added cholesterol to the formulations and studied the effect of each component (i.e., DPPC, Chol, Brij 78) on drug loading efficiency (%), size, zeta potential, polydispersity index, and transition temperature, as shown in Table 1 and Fig. S1 (in the Supplementary Data). Table 1 shows that DOX loading efficiency is >66% in all of liposomal formulations. In terms of the effect of cholesterol on the loading efficiency of DOX, we show that encapsulation efficacy increased from 77.1 ± 2.3 to 94.4 ± 1.8 by increasing the amount of cholesterol from 0% to 15% in the formulation that contained 0% Brij 78. Also, a similar trend in increase is evident in formulations containing 4% and 8% Brij 78. The encapsulation efficiency of formulations with 4% Brij78 increased from 78.1 ± 3.8% to 83.7 ± 3.6% and 88.4 ± 1.7% by increasing the cholesterol molar ratio from 0% to 10% and 15% in formulation content, respectively. The formulations that contained 8% Brij 78 increased from 66.4 ± 5.8% to 70.9 ± 2.8% and 75.3 ± 4.8% ($p < .05$). This increase in entrapment efficiency which can be attributed to an increase in membrane's rigidity and a reduction in the permeability of liposomes [56], in turn results in higher drug loading. It is evident from Table 1 that the encapsulation efficiency decreases significantly ($p < 0.05$) with increase in the Brij 78 M ratio for the same liposomal composition (e.g.: F1, F2 and F3). This may lead to an incompatibility between Brij 78 and DPPC which increases the drug leakage from the liposomal bilayer.

Table 1. The effect of liposome composition on drug loading, size, and zeta potential.

Formulation	DPPC: Brij 78: chol (molar ratio)	Load%	Size (nm)	Poly dispersity index (PDI)	Zeta potential (mV)	Transition pick (°C)
F1	1/0/0	77.1 ± 2.3	124.6 ± 6.3	0.25	−10.1 ± 0.1	42.9
F2	0.96/0.04/0	78.1 ± 3.8	115.3 ± 5.7	0.27	−13.0 ± 0.3	41.0

F3	0.92/0.08/0	66.4 ± 5.8	110.3 ± 4.2	0.28	−6.6 ± 2.3	37.8
F4	0.9/0/0.10	92.2 ± 1.3	130.8 ± 4.7	0.22	−9.6 ± 1.3	46.5
F5	0.86/0.04/0.10	83.7 ± 3.6	116.2 ± 6.8	0.19	−9.2 ± 1.6	41.6
F6	0.82/0.08/0.10	70.9 ± 2.8	114.7 ± 3.1	0.27	−8.5 ± 1.4	39.0
F7	0.85/0/0.15	94.4 ± 1.8	136.5 ± 5.3	0.22	−9.2 ± 1.3	50.5
F8	0.81/0.04/0.15	88.4 ± 1.7	129.6 ± 7.4	0.26	−7.3 ± 1.4	46.7
F9	0.77/0.08/0.15	75.3 ± 4.8	121.4 ± 6.7	0.248	−7.28 ± 2.28	43.08

Furthermore, from Table 1, it is observed that the mean particle diameter in all formulations is around 110–136 nm. This shows a good homogeneity in particle size among different molar ratios of the formulation. It is observable that the increase in the cholesterol composition increases the mean particle diameter for the same molar ratio of DPPC and Brij 78 (e.g.: F1, F4 and F7 are composed of 0% Brij 78). These observations can be attributed to the inclusion of cholesterol into the liposomal formulation which tends to eliminate transition temperature of DPPC. Hence, the chance of cholesterol remaining in the solid state increased, resulting in less dilution of the membrane and an increase in diameter [58]. As shown in Table 1, no significant differences in zeta potential or PDI were observed in all formulations.

3.2. Evaluation of glass transition temperature

We conducted DSC analysis to find the liposomal composition that resulted in optimal thermoresponsive functionality. As shown in Fig. S1 and Table 1, liposome composition influenced the DSC thermogram and led to a change in glass transition temperature. For liposomes composed only of DPPC, the glass transition temperature was 42.9 °C. The addition of cholesterol increased the transition temperature with a broadness of peak [59]. The highest transition temperature recorded by DSC was 50.5 °C in the formulation composed of DPPC/Chol (85/15). For liposomes composed of DPPC and Brij 78, the addition of Brij 78 decreased the glass transition temperature. As evident from the table, the lowest transition temperature was 37.83 °C for the formulation composed of DPPC/Brij 78 (92/8). In addition, the asymmetry glass transition peaks for F3, F6, and F9 showed that 8% of Brij 78 did not interact well with DPPC in lipid membrane so the phase transition temperature was more irregular than in F2, F5, and F8; which were composed of 4% Brij 78 [60]. Furthermore, the thermogram profiles of F2 and F3 showed a gel-to-liquid pre-transition between 31 °C and 37 °C leading to a premature drug leakage, while adding cholesterol (see F5 and F6) abolished DPPC pre-transition [61] thus increasing liposomal stability at 37 °C.

An ideal thermosensitive liposomes should exhibit a phase transition temperature at the therapeutic window for the application of hyperthermia (i.e., 41–45 °C) [59]. Hence, F3, F4, F7 and F8 cannot be considered as thermosensitive carriers. In the next section, we describe the in-vitro drug release assay used to further investigate the optimal liposomal formulation for hyperthermia therapy.

3.3. In vitro drug release assay

Formulation screening (see 3.1 Evaluation of Tlip formulation, 3.2 Evaluation of glass transition temperature) indicates that F1, F2, F5, F6, and F9 have promising thermal transition temperatures and loading efficiencies for consideration as thermosensitive liposome compositions. To further investigate the influence of Brij 78 and cholesterol on the temperature and time dependent drug release behavior of the formulations, we examined the drug release profile of each formulation at 37 °C and 42 °C (see Fig. 1A, B). In addition, Fig. 1C and D show drug release after 30 min at 37 °C and after 9 min at 42 °C, respectively.

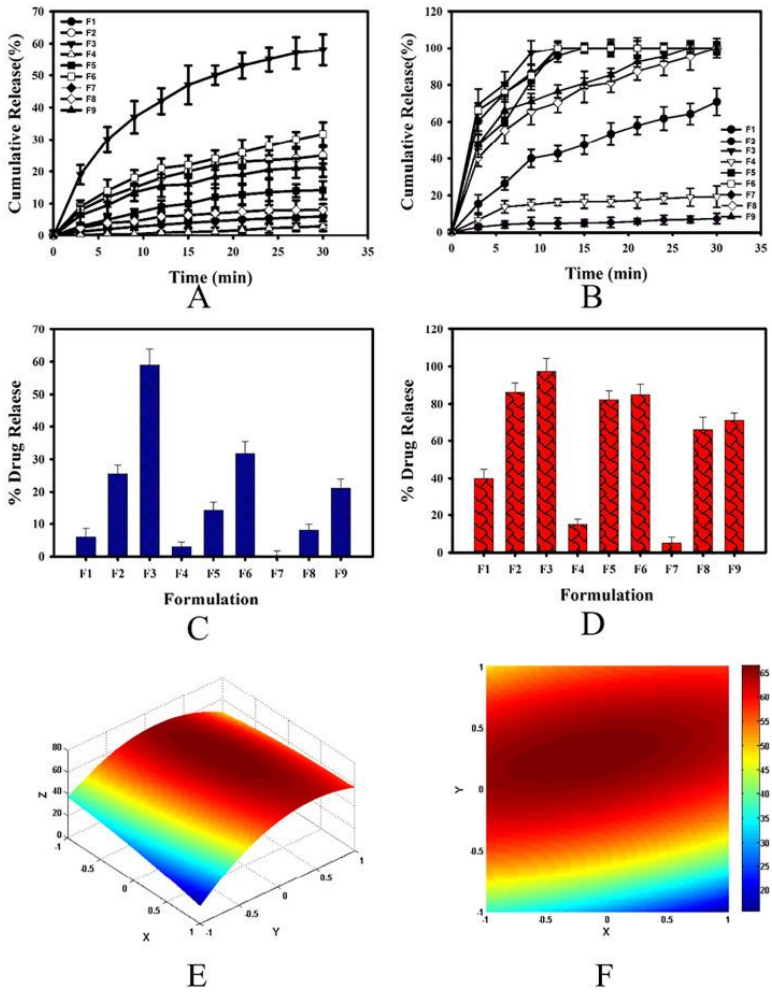

Fig. 1. Release profile of DOX from each formulation over 30 min at A) 37 °C and B) 42 °C. The percentage of drug release from each formulation C) after 30 min at 37 °C, and D) after 9 min at 42 °C. E) a 3-dimensional chart of experimental design for net release of DOX. F) a projection of E on the XY plane where X is the cholesterol molar ratio, Y is the Brij 78 M ratio, and Z is the net release (Re).

For liposomes composed only of DPPC, drug release after 30 min was 6.0 ± 2.7% and 70.9 ± 7.3% at 37 °C and 42 °C, respectively. Additional drug release at 37 °C and 42 °C was evident from the presence of Brij 78 in the composition (comparing F2 with F3, F5 with F6, and F8 with F9) [52]. Fig. 1C and D show that F2, F5, and F6 exhibit >80% drug release after 9 min of mild hyperthermia, and they exhibit 25.5 ± 2.6%, 14.2 ± 2.8%, and 31.7 ± 3.7% release after 30 min at 37 °C. It seems that the thermo-response of F2 and F6 are substantial, but the level of drug leakage at 37 °C is also substantial.

Adding cholesterol to the bilayer decreases drug leakage by decreasing the bilayer fluidity, but it also decreases the thermo-response of the vesicle [61]. However, the presence of Brij 78 improved thermo-response at 42 °C, but in excess amounts, it could negatively influence the stability of the bilayer at physiological temperatures. To optimize the amount of cholesterol and Brij 78, all formulations were subjected to a more detailed optimization using the CCD and RSM methods. We used the quadratic polynomial model to fine-tune the relationship between the Brij 78/ Chol molar ratio and net drug release. We assumed that the best formulation would exhibit a minimum amount of release after 30 min at 37 °C and maximum release after 9 min at 42 °C. This meant that the net release (R_e = amount of release after 9 min at 42 °C minus the amount of release after 30 min at 37 °C)

must be maximized. Table S1 shows the experimental results. Eq. (3) presents the proposed model on the regression coefficients:

(3) $f(x, y) = 64.52 - 2.979 * x + 13.08 * y - 2.583 * x^2 + 7.573 * x * y - 22.6 * y^2$

where *f*(*x*, *y*) is the net release, *x* is the molar ratio of cholesterol normalized by a mean of 0 and a standard deviation (STD) of 0.866, and *y* is the Brij 78 M ratio normalized by a mean of 0 and a STD of 0.866. Fig. 1E and F indicate the effect of the Brij 78/Chol molar ratio on net release. In the resulting model, the most efficient formulation was the liposomal formulation composed of 4.82% Brij 78 and 10.35% cholesterol, which is close to the F5 formulation.

3.4. Characterization of GO

Fig. 2A shows that, over the entire range of the IR spectrum, rGO has a greater optical density, specifically around the 800 nm wavelength (as shown in the inset) in comparison to probe-sonicated GO (small GO) and non-probe sonicated GO (large GO). This is attributed to the partial restoration of the π network of electrically insulated GO, which results in electronic conjugation among the reduced graphene sheets [62]. As shown in the inset, around a wavelength of 808 nm, the optical density of small GO was around 0.02, while after 2 h of probe sonication, it increased to 0.18. This may lead to an improvement in the GO dispersibility, in turn increase the photon absorption by the particles during NIR light irradiation.

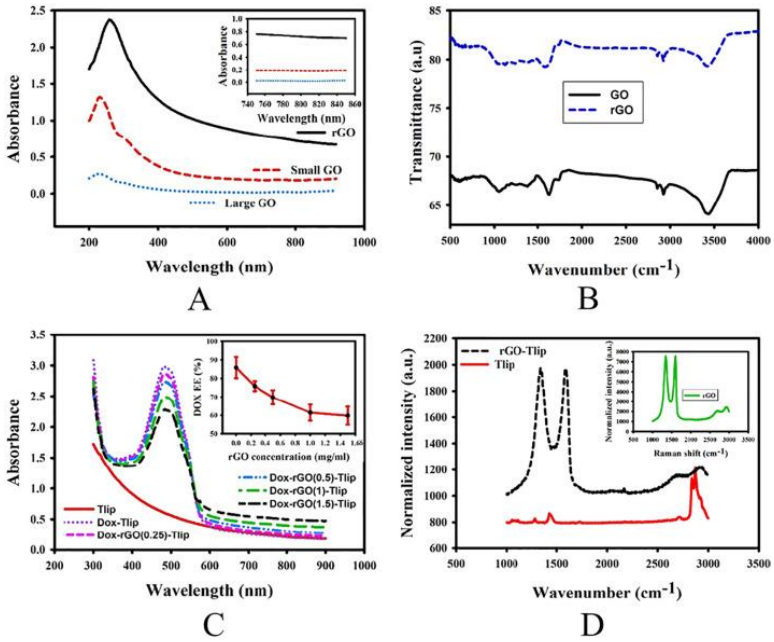

Fig. 2. A) UV–Vis spectrum of rGO and GO before and after probe sonication (inset shows the corresponding spectrum more specifically at around 800 nm). B) FTIR spectrum of rGO, GO. C) UV–Vis spectrum of Tlip, DOX-Tlip, rGO-Tlip, and DOX-rGO-Tlip with various concentrations of rGO (0.25, 0.5, 1, and 1.5 mg·ml^{-1}) (inset shows DOX encapsulation efficiency at different rGO concentrations). D) Raman spectroscopy of Tlip and rGO-Tlip (inset shows the Raman spectroscopy of rGO).

Moreover, a comparison of small GO, rGO, and aqueous GO suspensions displayed a strong peak at ~231 nm (π–π of aromatic carbon bonds). For rGO suspension in water, the absorption shifts upward to ~261 nm because of the removal of oxygen-containing group during reduction. Moreover, absorption cross-section of the rGO is an important parameter describing the ability of transducer to absorb incident light as described in Supplementary

3. The absorption cross-section of rGO is 45.12±4.24 [$\frac{\mathrm{ml}}{\mathrm{mg \cdot cm}}$] which is close to the value that previously reported for rGO-Arg by Hashemi et al. [35].

To further confirm GO reduction, we conducted FTIR analysis for GO and rGO. The GO spectrum showed the presence of $\mathrm{O-H}$ (at 3386 cm^{-1}), $\mathrm{C=O}$ (at 1733 cm^{-1}), $\mathrm{C=C}$ (at 1622 cm^{-1}), and $\mathrm{C-O}$ (at 1129 cm^{-1}). Meanwhile, the elimination of oxide group–related peaks in rGO indicates full reduction of GO.

3.5. Characterization of self-assembled DOX-rGO-Tlip nanohybrids

Recently, self-assembly of the materials have absorbed a great deal of attention in the biomedical engineering. For example, Shi et al. synthesized artificial proto-osteocells composed of biphasic calcium phosphates encapsulated BMP2 stabilized Pickering emulsions [63].

In this study, self-assembled rGO-Tlip nanohybrids were synthesized using the thin-film hydration method followed by probe sonication to reduce the size of the rGO-Tlip. Size reduction by extrusion was not appropriate, since rGO is removed by the polycarbonate filter. We conducted UV spectroscopy to evaluate the encapsulation efficiency and the incorporation efficiency of DOX and rGO, respectively, in the DOX-rGO-Tlip. The encapsulation efficiency of the formulation composed of DPPC: Chol: Brij 78 (84.82:10.35:4.83 M ratio – $Tlip_{opt}$) was 85.83 ± 5.69%, based on optimization in Section 3.3. Adding 0.25 $mg \cdot ml^{-1}$ of rGO to the formulation, DOX encapsulation efficiency decreased to 75.8 ± 2.7% (Fig. 2C). Increasing the incorporation of rGO, DOX encapsulation efficiency decreased (Fig. 2C, inset) ($p < .05$). This may lead to an increase in vesicular incompatibility between lipids and rGO, causing defect formation in the bilayer and a decrease the encapsulation efficiency of the drug. As the results show, adding 1 $mg \cdot ml^{-1}$ of rGO to the liposomal formulation, DOX encapsulation efficiency decreased to 61.39 ± 4.3%.

We used UV–Vis spectroscopy to analyze the washing solution representing rGO incorporation efficiency in the rGO-Tlip formulation. The rGO incorporation efficiency was 30.4 ± 5.6%, 40.5 ± 3.9%, 47.8 ± 4.8%, and 58.8 ± 4.7% in the presence of 1.5, 1, 0.5, and 0.25 $mg \cdot ml^{-1}$ of rGO, respectively.

Raman spectroscopy confirmed the presence of rGO in the liposomal structure and also monitored defect formation during the self-assembly of rGO-Tlip (Fig. 2D). Two obvious bands located in the rGO-Tlip at around 1350 cm^{-1} and 1590 cm^{-1} assigned the G band and D band corresponding rGO structure in the liposomal formulation. The ratio of the intensity of the D band to the G band was consistent with the structural defect in rGO. As shown in Fig. 2D, the number of defects (I_D/I_G), did not change during self-assembly [64].

The morphology of the rGO-Tlip was characterized by SEM, as shown in Fig. 3. Before the rGO-Tlip formation, rGO nanosheets (Fig. 3C) were in the flat shape. While during the self-assembly of Tlip and rGO, rGOs interacted with the hydrophobic parts of Tlips membrane resulting to change the morphology and collapse on the surface of the liposomes (Fig. 3A) and create a flower-shaped nanohybrid of rGO-Tlip (Fig. 3B).

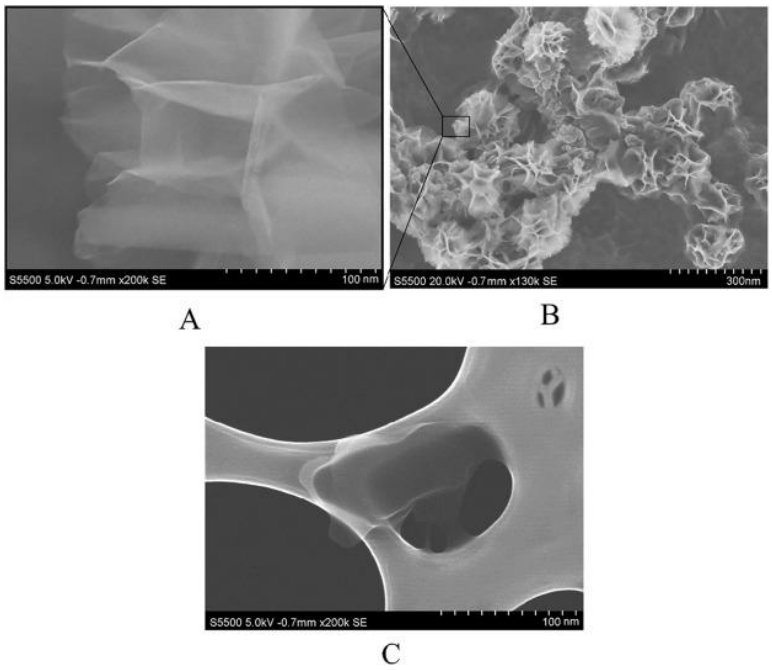

Fig. 3. SEM spectroscopy of A) rGO on the surface of rGO-Tlip, B) rGO-Tlip, C) rGO.

Also, we need to mention that aggregation occurred during the drying process and the suspension was well synthesized. Also, DLS analysis showed that the size of rGO-Tlip increased from 112.9 ± 5.39 nm to 190.54 ± 10.39 nm as a result of the self-assembly of rGO and Tlip. This novel shape may have been created due to the hydrophobic interaction of the rGO nanosheets and the lipid bilayer of Tlip.

3.6. Study CQD and DOX interaction

The PL intensity of theranostic system composed of CQD encapsulated DOX-rGO-Tlip were studied in Fig. 4A. The interaction of CQD and DOX inside the thermosensitive liposome might be through π-π stacking, hydrophobic interaction, electrostatic attraction and van der Waals force which is similar to the interaction of the other carbon-based materials [38,65,66]. At an excitation wavelength of 280 nm, the maximum emission of CQD and DOX are 426 and 600, respectively. The co-encapsulation of CQD and DOX inside the liposome (DOX-rGO-Tlip) was implied by the characteristic absorption peak of CQD and DOX at 426 and 600 nm, respectively, in the PL spectra of CQD-DOX-rGO-Tlip. This confirms a successful loading of both CQD and DOX inside the liposomes. Furthermore, an absorption band of DOX overlapped with the emission band of CQD at 426 nm, quenching the CQD emission through a FRET process. Moreover, the emission peak at 600 nm is much more intense for CQD-DOX-rGO-Tlip than that for DOX. A possible explanation is that CQD emission at 426 nm, quenched by absorption of DOX, may further strengthen the intensity of emission at 600 nm of DOX molecule, similar to results reported by Xiaojuan et al., [38] and Bagalkot et al., [67]. Xiaojuan et al., introduced hollow carbon dot for anticancer drug nanocarrier for DOX [38] and Bagalkot et al. attached RNA aptamer to CdSe/ZnS quantum dots loaded DOX molecule [67].

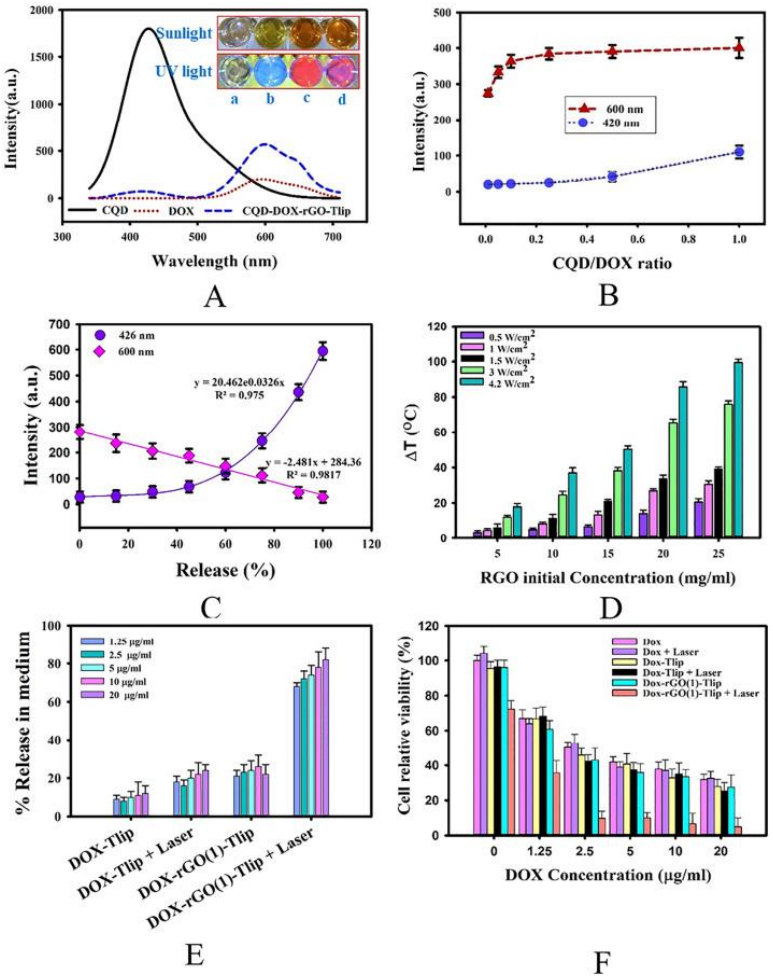

Fig. 4. A) Fluorescence spectra of CQD, DOX and DOX-rGO-Tlip with 280 nm excitation wavelengths (inset is a photograph of a: PBS, b: CQD, c: CQD-DOX-rGO(1)-Tlip, d: DOX-rGO(1)-Tlip, B) PL emission of different mass ratio of CQD/DOX with 280 nm excitation wavelengths. C) Evaluation of % release of CQD-DOX-rGO(1)-Tlip based on PL intensity with 280 nm excitation at 420 and 600 nm emission wavelength. D) Temperature difference curve at various incident NIR laser fluences (0.5, 1, 1.5, 3, and 4.2 $W \cdot cm^{-2}$) for various rGO concentrations (0.25, 0.5, 1, 1.5 $mg \cdot ml^{-1}$). E) % release of DOX from DOX-Tlip and DOX-rGO(1)-Tlip with or without NIR laser irradiation (5 min, 1 $W \cdot cm^{-2}$). F) Cell viabilities of MD-MB-231 cells after incubation with DOX, DOX-Tlip, DOX-rGO(1) -Tlip, and DOX-rGO-Tlip with or without NIR pulsed laser irradiation (5 min, 1 $W \cdot cm^{-2}$).

The inset picture of Fig. 4A represents the photograph of PBS (a), CQD (b), DOX-rGO(1)-Tlip + CQD (c) and DOX-rGO(1)-Tlip (d) under UV and sunlight excitation. CQD showed blue and light brown color under UV and sun light, respectively, while there was no change in PBS color. Although the color of CQD encapsulated DOX-rGO-Tlip (c) and DOX-rGO-Tlip(d) are the same under sunlight emission, there were an obvious color changed under UV light emission.

On further investigation, we observed that the fluorescence of CQD/DOX mixture increased as we increased the CQD/DOX mass ratio to 0.2, keeping DOX concentration fixed, suggesting the fluorescence is from the larger population of CQD molecules. Above this mass ratio of 0.2, the fluorescence reached almost a plateau. This observation which is due to the dynamic/static quenching effect [68], is in accordance with result reported by Xiaojuan et al. [38]. Fig. 4B depicts the fluorescent emission intensity at 420 and 600 nm in terms of CQD/DOX mass ratio ranging 0–1, keeping DOX concentration fixed and increasing CQD concentration gradually. At

600 nm, the intensity at a mass ratio of 0 acts as the starting value, only related to the presence of DOX molecules.

Co-encapsulation of DOX and CQD in a single platform provides a unique feature to in vitro and in vivo monitoring drug release. It has to be noted that to find a relationship between DOX and CQD release profile, the mass ratio of CQD/DOX should be below 0.2 (prior to saturation as seen in Fig. 4B). To evaluate the potential application of online monitoring drug release, the emission intensity of CQD while DOX released from the nanohybrid vesicles were measured at certain time intervals. As shown in Fig. 4C, the emission spectra at 420 and 600 nm increased and decreased, respectively with increasing DOX release. This observation may help to decrease the quenching effect at 426 nm and consequently decreasing the FRET effect at 600 nm observed with increasing DOX release.

3.7. Photothermal and in vitro characteristics of CQD-DOX-RGO-Tlip

We explored the photothermal properties of CQD-DOX-rGO-Tlip at various initial rGO concentrations (0.25, 0.5, 1, and 1.5 $mg \cdot ml^{-1}$), and the rise in temperature of CQD-DOX-rGO-Tlip was determined under NIR pulsed irradiation with different power densities (0.5, 1, 1.5, 3, 4.2 $W \cdot cm^{-2}$) after 5 min. As shown in Fig. 4D, in all the samples, the temperature increased as expected with increase in laser power density, owing to an increase in input energy. It is clear that all samples demonstrated concentration-dependent temperature increase in response to NIR irradiation. After 5 min of irradiation by the NIR pulse laser with a power density of 1 $W \cdot cm^{-2}$, the temperature increase of DOX-rGO(1)-Tlip and DOX-rGO(1.5)-Tlip increased to 26.84 ± 1.1 °C and 30.45 ± 1.8 °C, respectively. However, the temperature increase for DOX-Tlip, as a control solution, was far less (4.4 ± 1 °C). As the DOX loading efficiency decreased significantly in DOX-rGO(1.5)-Tlip as mentioned earlier, the formulation composed of 1 $mg \cdot ml^{-1}$ of rGO (DOX-rGO(1)-Tlip) was selected for further study.

As shown in Fig. 4E, to obtain the exact amount of DOX exposed to MD-MB-231 cell lines, the PL of CQD-DOX-Tlip and CQD-DOX-rGO-Tlip at various DOX concentration with or without NIR laser irradiation (5 min, 1 $W \cdot cm^{-2}$) were measured (280 nm excitation/600 nm emission) and compared to Fig. 4C.

Then, we studied the in vitro photothermal properties of DOX-rGO(1)-Tlip on MD-MB-231 by MTT assays, after 5 min of exposure to an NIR laser (1 $W \cdot cm^{-2}$). As shown in Fig. 4F, the cells were treated with different concentrations of DOX in the form of free DOX, DOX-Tlip, and DOX-rGO(1)-Tlip, with or without laser emission. The data represent a relatively lower cell viability of 5.3 ± 5.8% in the DOX-rGO(1)-Tlip sample treated by laser emission, compared to the cell viability of the system without laser treatment (27.9 ± 6.3%). Moreover, the toxicity of DOX-rGO(1)-Tlip with NIR laser emission considerably increased in comparison to free DOX or DOX-Tlip ($p < .05$). Furthermore, when MD-MB-231 cells were treated by DOX and DOX-Tlip with laser irradiation, the change in toxicity was not significant, compared to the group not exposed to laser irradiation ($p < .05$). Also, MTT assays with no nanoparticles in the cell culture medium revealed a negligible amount of cell toxicity after 5 min of laser irradiation. These results suggest that DOX-rGO(1)-Tlip in the concentration of 10 $\mu g \cdot ml^{-1}$ of initial DOX concentration (7.8 $\mu g \cdot ml^{-1}$ exposed to MD-MB-231 (calculated using Fig. 4E)) can provide almost 100% toxicity against the MD-MB-231 cell line.

As a supplementary examination of the photochemotherapy potential of DOX-rGO(1)-Tlip, we conducted a live/dead assay using calcein AM/EthD–1, as shown in Fig. 5. MD-MB-231 cells were treated with DOX-rGO-Tlip for 24 h. After NIR laser emission (1 $W \cdot cm^{-2}$), cells were stained and immediately examined under fluorescence microscopy.

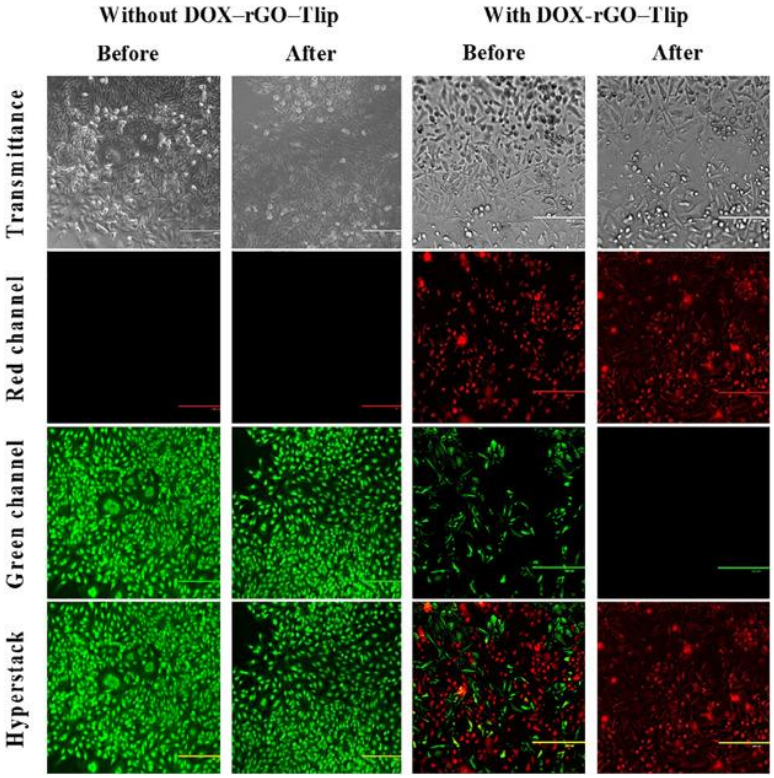

Fig. 5. Live/dead assay of MD-MB-231 cell line with and without of DOX-rGO(1)-Tlip before and after 5 min of NIR pulsed laser irradiation (1 W·cm^{-1}). Green channel: live cells. Red channel: dead cells. Hyperstack: a merging of both channels (the scale bar is 200 μm). (For interpretation of the references to color in this figure legend, the reader is referred to the web version of this article.)

In the group treated with DOX-rGO-Tlip, the toxicity (red spot) before laser emission was related to the chemotherapy effect of DOX, while after laser emission, an increase in the red spot related to both the photothermal and the chemotherapeutic effect of DOX-rGO-Tlip. As shown in Fig. 5, no significant change in toxicity level was observed in the samples, with no nanoparticles before and after laser emission. These results demonstrate the efficient chemo-photothermal therapy effect of DOX-rGO-Tlip in destroying MD-MB-231 breast cancer cell lines.

DOX-rGO-Tlip with NIR laser emission provides dual-mode chemotherapy and photothermal therapy. First, NIR is absorbed by rGO and converted to heat. Then, the heat activated gel-to-liquid phase transition of the phospholipid membrane leading to the release of the encapsulated toxic drug. At the same time, the heat absorbed by rGO could provide a photothermal therapeutic effect. Both modes are localized, which reduces the side effects compared to traditional cancer treatment [15].

3.8. Confocal microscopic and flow cytometry characterization of cellular uptake

In this study, to achieve an effective photothermal therapy, flow cytometry and confocal microscopy have been used to evaluate the cellular uptake of CQD-rGO-Tlip into MD-MB-231 cell lines over 0, 4, and 24 h (Fig. 6).

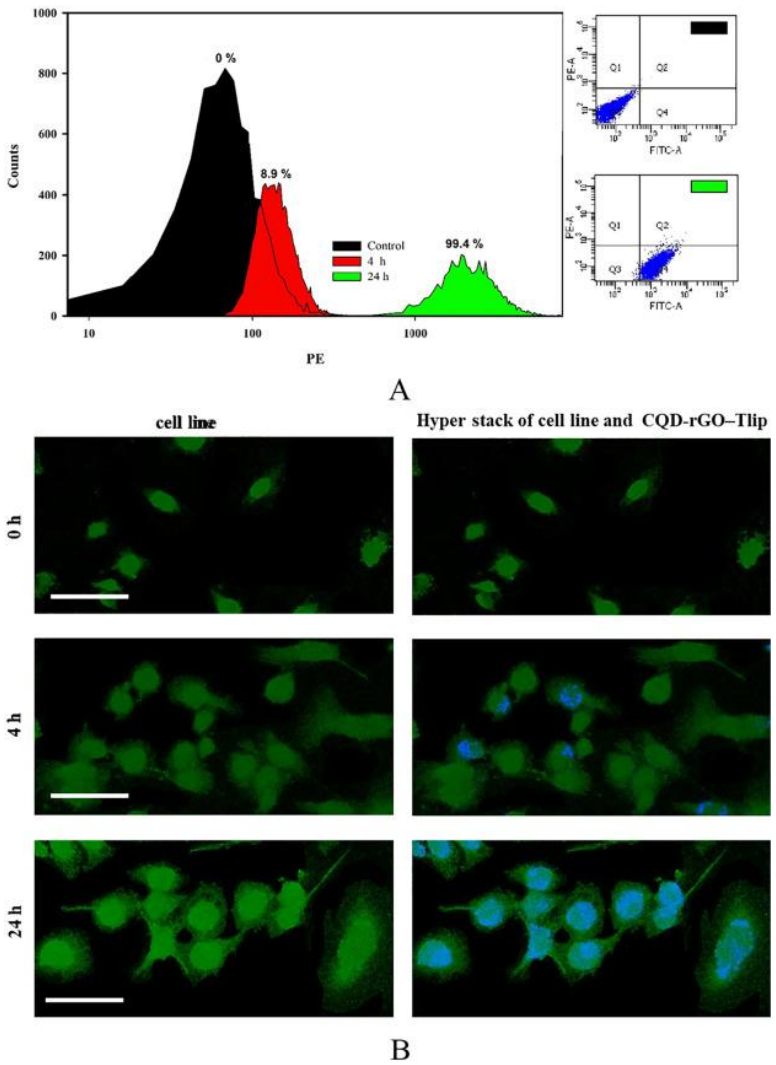

Fig. 6. The intracellular uptake of rGO-Tlip in MD-MB-231 cell lines was observed by A) flow cytometry after 0, 2, and 24 h and B) confocal microscopy. Green: cytoplasm. Blue: CQD-rGO-Tlip. (scale bar is 50 μm). (For interpretation of the references to color in this figure legend, the reader is referred to the web version of this article.)

Flow cytometry analysis showed a highly efficient and time-dependent intracellular delivery (Fig. 6A). In addition, confocal microscopy analysis showed that CQD-rGO-Tlip uptake was consistent with flow cytometry data (Fig. 6B). The gradual increase in the intensity of blue fluorescence, which indicates the presence of CQD, implies a high intracellular uptake capability of CQD-rGO-Tlip. The ability of CQDs to be taken up by the cells are mainly due to their small size leading to the readily uptake [39], while in the CQD-rGO-Tlip the cellular uptake was related to the nature of the liposomes.

As previously reported by Gabizon et al., it is worth to note that the presence of Brij 78, a surfactant composed of an acyl chain with a terminal PEG, could reassemble the structure of DSPE-PEG 2000 and the single-chain phospholipid in the thermosensitive formulation [55]. Thus, the presence of Brij 78 in the rGO-Tlip nanohybrids could increase blood circulation and consequently increase the endocytic uptake of rGO-Tlip [69].

3.9. In vivo photothermal therapy

Motivated by high in vitro toxicity and strong tumor accumulation of CQD-DOX-rGO-Tlip in tumorogenic cells, an initial study on in vivo photothermal therapy was conducted. It should be noted that the diagnostic aspect of

using CQD-DOX-rGO-Tlip in animal models will need further studies. As shown in Fig. 7A, the tumor of mice treated by CQD-DOX-rGO(1)-Tlips disappeared 30 days after NIR pulsed laser irradiation (Fig. 7B), while control groups had rapid tumor growth (Fig. 7A and B). Also, even for those groups treated by CQD-DOX-rGO(1)-Tlips, the photothermal therapy was not efficient. Similar results were reported by Kai et al., after treating mice bearing 4T1 tumors with nRGO-PEG [50].

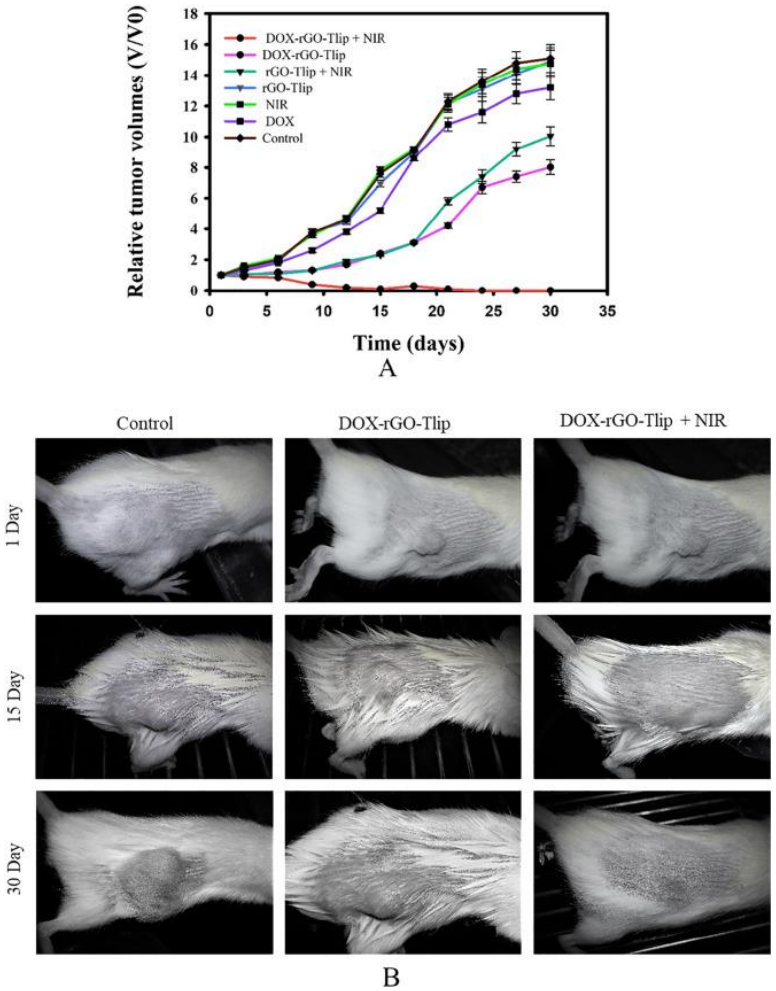

Fig. 7. Animal study of chemo-photothermal potential of DOX-rGO-Tlip. A) Tumor growth profile of different groups treated with or without NIR pulsed laser irradiation (1 W·cm^{-2}), the tumor volume was normalized to the initial tumor volume. B) Photograph of tumor-bearing mice treated by CQD-DOX-rGO-Tlip with or without NIR pulsed laser irradiation.

4. Conclusion

CQD-DOX-rGO-Tlip, a dual chemo-photothermal theranostic platform, was successfully prepared by incorporation of rGO into the bilayer and encapsulation of synthesized CQD and DOX inside the Tlip during self-assembling of Tlip. The rGO embedded in the bilayer functions as a heat absorbing agent and the thermoresponsive liposomal nanoparticles exhibited a high loading capacity for both DOX and CQD. Also, the presence of Brij 78 in the Tlip can increase blood circulation. Moreover, the presence of CQD inside the DOX-rGO-Tlip provided a potential application of tumor imaging and online monitoring of DOX release. We demonstrated that this system has potential for chemo-photothermal theranostic application.

Declaration of Competing Interest

There is no conflict of interest to declare.

Acknowledgments

The work support by the Cancer Prevention Research Institute of Texas (CPRIT) grant DP150102.The

Appendix A. Supplementary data

Download : **Download Acrobat PDF file (1MB)**

Supplementary material

References

[1] M. Guan, H. Dong, J. Ge, D. Chen, L. Sun, S. Li, C. Wang, C. Yan, P. Wang, C. Shu. NPG Asia Materials, 7 (2015), p. e205

[2] H. Wang, P. Agarwal, S. Zhao, J. Yu, X. Lu, X. He, Nat. Commun. (2015), p. 6

[3] Q. Chen, H. Ke, Z. Dai, Z. Liu, Biomaterials, 73 (2015), pp. 214-230

[4] S.S. Kelkar, T.M. Reineke, Bioconjug. Chem., 22 (2011), pp. 1879-1903

[5] H.K. Moon, S.H. Lee, H.C. Choi, ACS Nano, 3 (2009), pp. 3707-3713

[6] M. Fahmy, H. Jazayeri, M. Razavi, M. Hashemi, M. Omidi, M. Farahani, E. Salahinejad, A. Yadegari, S. Pitcher, L. Tayebi, Intelligent Nanomaterials (2016), p. 199

[7] J. Wang, E. Ayano, Y. Maitani, H. Kanazawa, Int. J. Pharm., 523 (2017), pp. 217-228

[8] V.P. Torchilin, Nat. Rev. Drug Discov., 13 (2014), p. 813

[9] M. Liu, H. Du, W. Zhang, G. Zhai, Mater. Sci. Eng. C, 71 (2017), pp. 1267-1280

[10] F. Mahmoodzadeh, M. Abbasian, M. Jaymand, R. Salehi, E. Bagherzadeh-Khajehmarjan, Mater. Sci. Eng. C, 93 (2018), pp. 880-889

[11] P. Huang, J. Lin, W. Li, P. Rong, Z. Wang, S. Wang, X. Wang, X. Sun, M. Aronova, G. Niu, Angew. Chem., 125 (2013), pp. 14208-14214

[12] Y. Tang, A.J. McGoron, J. Photochem. Photobiol. B Biol., 97 (2009), pp. 138-144

[13] L.R. Hirsch, R.J. Stafford, J. Bankson, S.R. Sershen, B. Rivera, R. Price, J.D. Hazle, N.J. Halas, J.L. West, Proc. Natl. Acad. Sci., 100 (2003), pp. 13549-13554

[14] E.B. Dickerson, E.C. Dreaden, X. Huang, I.H. El-Sayed, H. Chu, S. Pushpanketh, J.F. McDonald, M.A. El-Sayed, Cancer Lett., 269 (2008), pp. 57-66

[15] L. Tong, Q. Wei, A. Wei, J.X. Cheng, Photochem. Photobiol., 85 (2009), pp. 21-32

[16] V. Sharma, K. Park, M. Srinivasarao, Materials Science and Engineering: R: Reports, 65 (2009), pp. 1-38

[17] N. Zhang, X. Xu, X. Zhang, D. Qu, L. Xue, R. Mo, C. Zhang, Int. J. Pharm., 497 (2016), pp. 210-221

[18] N.W.S. Kam, M. O'Connell, J.A. Wisdom, H. Dai, Proc. Natl. Acad. Sci. U. S. A., 102 (2005), pp. 11600-11605

[19] M.S. Khan, H.N. Abdelhamid, H.-F. Wu, Colloids Surf. B: Biointerfaces, 127 (2015), pp. 281-291

[20] V.N. Popov, Materials Science and Engineering: R: Reports, 43 (2004), pp. 61-102

[21] Z. Li, A.L.B. de Barros, D.C.F. Soares, S.N. Moss, L. Alisaraie, Int. J. Pharm., 524 (2017), pp. 41-54

[22] O.C. Compton, S.T. Nguyen, small, 6 (2010), pp. 711-723

[23] B. Zhang, Y. Wang, G. Zhai, Mater. Sci. Eng. C, 61 (2016), pp. 953-964

[24] M. Omidi, A. Fathinia, M. Farahani, Z. Niknam, A. Yadegari, M. Hashemi, H. Jazayeri, H. Zali, M. Zahedinik, L. Tayebi, **Advanced 2D Materials,** (2016), pp. 433-471

[25] T.A. Pham, B.C. Choi, K.T. Lim, Y.T. Jeong, Appl. Surf. Sci., 257 (2011), pp. 3350-3357

[26] T. Miyazaki, J. Akaike, M. Kawashita, H.N. Lim, Mater. Sci. Eng. C, 99 (2019), pp. 68-72

[27] N.K. Kadiyala, B.K. Mandal, S. Ranjan, N. Dasgupta, Mater. Sci. Eng. C, 93 (2018), pp. 191-205

[28] A.A. Yakout, M.E. Mahmoud, Mater. Sci. Eng. C, 92 (2018), pp. 287-296

[29] K. Yang, S. Zhang, G. Zhang, X. Sun, S.-T. Lee, Z. Liu, Nano Lett., 10 (2010), pp. 3318-3323

[30] J.T. Robinson, S.M. Tabakman, Y. Liang, H. Wang, H. Sanchez Casalongue, D. Vinh, H. Dai, J. Am. Chem. Soc., 133 (2011), pp. 6825-6831
[31] H. Hu, X. Wang, K.I. Lee, K. Ma, H. Hu, J.H. Xin, Sci. Rep. (2016), p. 6
[32] L. Zhang, Z. Wang, Z. Lu, H. Shen, J. Huang, Q. Zhao, M. Liu, N. He, Z. Zhang, J. Mater. Chem. B, 1 (2013), pp. 749-755
[33] R. Imani, W. Shao, S.H. Emami, S. Faghihi, S. Prakash, RSC Adv., 6 (2016), pp. 77818-77829
[34] M. Hashemi, A. Yadegari, G. Yazdanpanah, S. Jabbehdari, M. Omidi, L. Tayebi, RSC Adv., 6 (2016), pp. 74072-74084
[35] M. Hashemi, M. Omidi, B. Muralidharan, H. Smyth, M.A. Mohagheghi, J. Mohammadi, T.E. Milner, ACS Appl. Mater. Interfaces, 9 (2017), pp. 32607-32620
[36] J. Yang, J.-H. Yu, J.R. Strickler, W.-J. Chang, S. Gunasekaran, Biosens. Bioelectron., 47 (2013) 530–538.
[37] H.-S. Cho, Z. Dong, G.M. Pauletti, J. Zhang, H. Xu, H. Gu, L. Wang, R.C. Ewing, C. Huth, F. Wang, ACS Nano, 4 (2010), pp. 5398-5404
[38] X. Gong, Q. Zhang, Y. Gao, S. Shuang, M.M. Choi, C. Dong, ACS Appl. Mater. Interfaces, 8 (2016), pp. 11288-11297
[39] X.T. Zheng, A. Ananthanarayanan, K.Q. Luo, P. Chen, Small, 11 (2015), pp. 1620-1636
[40] Y.-P. Sun, B. Zhou, Y. Lin, W. Wang, K.S. Fernando, P. Pathak, M.J. Meziani, B.A. Harruff, X. Wang, H. Wang, J. Am. Chem. Soc., 128 (2006), pp. 7756-7757
[41] S.-T. Yang, L. Cao, P.G. Luo, F. Lu, X. Wang, H. Wang, M.J. Meziani, Y. Liu, G. Qi, Y.-P. Sun, J. Am. Chem. Soc., 131 (2009), pp. 11308-11309
[42] H. Tao, K. Yang, Z. Ma, J. Wan, Y. Zhang, Z. Kang, Z. Liu, Small, 8 (2012), pp. 281-290
[43] Q. Liu, B. Guo, Z. Rao, B. Zhang, J.R. Gong, Nano Lett., 13 (2013), pp. 2436-2441
[44] H. Dehaghi, S.D. Zadeh, H. Keshvari, P. Abasian, Research in Pharmaceutical Sciences, 7 (2012), p. S290
[45] M. Hashemi, M. Omidi, B. Muralidharan, L. Tayebi, M.J. Herpin, M.A. Mohagheghi, J. Mohammadi, H.D. S myth, T.E. Milner, Acta Biomater., 65 (2018), pp. 376-392
[46] M. Omidi, A. Yadegari, L. Tayebi, RSC Adv., 7 (2017), pp. 10638-10649
[47] A. Rashidi, B. Ghobadian, G. Najafi, M.H. Khoshtaghaza, N.A.C. Sidik, A. Yadegari, H.W. Xian, International Communications in Heat and Mass Transfer, 90 (2018), pp. 85-92
[48] A. Rashidi, A. Yadegari, E. Ettefaghi, S. Khodabakhshi, R. Lotfi, M. Rashtchi, Google Patents, 2017.
[49] L. Xiong, B. Shen, D. Behera, S.S. Gambhir, F.T. Chin, J. Rao, Nanoscale, 5 (2013), pp. 3253-3256
[50] K. Yang, J. Wan, S. Zhang, B. Tian, Y. Zhang, Z. Liu, Biomaterials, 33 (2012), pp. 2206-2214
[51] J.K. Mills, D. Needham, Biochimica et Biophysica Acta (BBA)-Biomembranes, 1716 (2005), pp. 77-96
[52] T. Tagami, M.J. Ernsting, S.-D. Li, J. Control. Release, 154 (2011), pp. 290-297
[53] D. Needham, J.-Y. Park, A.M. Wright, J. Tong, Faraday Discuss., 161 (2013), pp. 515-534
[54] G.N. Chiu, S.A. Abraham, L.M. Ickenstein, R. Ng, G. Karlsson, K. Edwards, E.K. Wasan, M.B. Bally, J. Control. Release, 104 (2005), pp. 271-288
[55] T. Tagami, M.J. Ernsting, S.-D. Li, J. Control. Release, 152 (2011), pp. 303-309
[56] M.-L. Briuglia, C. Rotella, A. McFarlane, D.A. Lamprou, Drug delivery and translational research, 5 (2015), pp. 231-242
[57] W. Shinoda, Biochimica et Biophysica Acta (BBA)-Biomembranes, 1858 (2016), pp. 2254-2265
[58] S.M. Park, M.S. Kim, S.-J. Park, E.S. Park, K.-S. Choi, Y.-s. Kim, H.R. Kim, J. Control. Release, 170 (2013), pp. 373-379
[59] T. Ta, T.M. Porter, J. Control. Release, 169 (2013), pp. 112-125
[60] J. Chen, D. Cheng, J. Li, Y. Wang, J.-x. Guo, Z.-p. Chen, B.-c. Cai, T. Yang, Drug Dev. Ind. Pharm., 39 (2013), pp. 197-204
[61] M.R. Krause, S.L. Regen, Acc. Chem. Res., 47 (2014), pp. 3512-3521
[62] D. Li, R.B. Kaner, Nat. Nanotechnol., 3 (2008), p. 101
[63] M. Shi, R. Yang, Q. Li, K. Lv, R.J. Miron, J. Sun, M. Li, Y. Zhang, ACS Appl. Mater. Interfaces, 10 (2018), pp. 10718-10728

[64] M. Hashemi, A. Yadegari, G. Yazdanpanah, M. Omidi, S. Jabbehdari, F. Haghiralsadat, F. Yazdian, L. Tayebi, Biotechnol. Appl. Biochem., 64 (3) (2017), pp. 433-442
[65] L. Zhang, J. Xia, Q. Zhao, L. Liu, Z. Zhang, Small, 6 (2010), pp. 537-544
[66] Z. Wang, Z. Tian, Y. Dong, L. Li, L. Tian, Y. Li, B. Yang, Diam. Relat. Mater., 58 (2015), pp. 84-93
[67] V. Bagalkot, L. Zhang, E. Levy-Nissenbaum, S. Jon, P.W. Kantoff, R. Langer, O.C. Farokhzad, Nano Lett., 7 (2007), pp. 3065-3070
[68] N.S.H. Motlagh, P. Parvin, F. Ghasemi, F. Atyabi, Biomedical optics express, 7 (2016), pp. 2400-2406
[69] M. Fazel, M. Daeihamed, M. Osouli, A. Almasi, A. Haeri, S. Dadashzadeh, Iranian journal of pharmaceutical research: IJPR, 17 (2018), p. 33